Design and Optimization of a Pole Changing Flux Switching Permanent Magnet Motor

Mao, Yi; Du, Yi; Xiao, Feng; Zhu, Xiaoyong; Quan, Li; Zhou, Dao

Published in:
I E E E Transactions on Industrial Electronics

DOI (link to publication from Publisher):
10.1109/TIE.2023.3237886

Publication date:
2023

Document Version
Accepted author manuscript, peer reviewed version

Design and Optimization of a Pole Changing Flux Switching Permanent Magnet Motor

Yi Mao, *Student Member*, *IEEE*, Yi Du, *Member*, *IEEE*, Feng Xiao, Xiaoyong Zhu, *Member*, *IEEE*, and Li Quan

***Abstract*—A flux switching permanent magnet (FSPM) motor is designed and optimized in this paper to achieve high torque density and expanded speed regulation range from a design viewpoint of pole-changing (PC). Based on the field modulation theory, the PM field in the FSPM motor is modulated by the stator and rotor teeth, generating rich harmonics with different pole-pair numbers in the air-gap flux density. By adopting an appropriate slot pole combination, working harmonics with different slot pitch angles are obtained to establish a basic of the PC-FSPM motor. Then, different working harmonics can be used to achieve different energy conversions with different winding configurations, so the PC operation can be performed to realize the high torque and wide speed regulation range by switching the working modes. Based on the field modulation theory, the operation principle of conventional and PC-FSPM motors are analyzed and compared. Then, according to the design principle of PC-FSPM motor, a 24/22-pole PC-FSPM motor with E-core is designed and optimized by a multi-level optimization method. Finally, the electromagnetic performances are analyzed by finite element analysis and the test results of the prototype verified the feasibility of the motor.**

***Index Terms*—Air-gap field modulation, flux switching permanent magnet motor, pole changing, wide speed regulation range.**

I. Introduction

FLUX switching (FS) permanent magnet (PM) motor has attracted much attention due to the advantages of simple rotor structure, easy temperature management, high torque density and efficiency [1]-[3]. However, the contradiction between the torque density in constant torque region and the speed regulation range in flux-weakening region limits the applications of FSPM motor, particularly for traction and propulsion applications, such as electric vehicles [4]. Hence, some efforts have been made to perform an adjustable excitation field, so as to obtain different novel FSPM motors with widened speed range, such as the hybrid excitation FSPM motor with both PMs and DC field windings [5]-[7], the FSPM memory motor with low coercive force (LCF) PMs [8], and the mechanical flux-weakening FSPM motor with moveable mechanical units [9]. However, the reported structures are complex, leading to high design and machine difficulties.

The synchronous speed is proportional to the pole-pair number, so the speed regulation range can be extended by pole-changing (PC) operation. Based on the PC concept, three kinds of PC motor have been reported, including the PC induction motor (PC-IM) [10]-[15], the PC dual-speed PM motor (PC-DSPMM) [16]-[18], and the PC memory motor (PC-MM) [19][20].

The PC-IM has been widely commercialized for the grid-connected condition. Based on the adoption of a squirrel cage rotor [10]-[13] or a wound rotor [14][15], the rotor field is generated by the electromagnetic induction on armature field, so the pole-pair number of rotor field is always consistent with the armature one. Therefore, the PC operation of PC-IM can be performed once the armature winding connection is changed to obtain the stator armature field with different pole-pair numbers.

By employing hybrid rotor structures, the rotor excitation field of PC-DSPMMs contains two components with different pole-pair numbers. So, this kind of motor can realize dual-speed operation with the grid-connection by changing its winding connection. Several different hybrid rotor structures have been proposed for the PC-DSPMM, such as, the hybrid rotor with both a cage and 4-pole PMs [16], the hybrid rotor with 4-pole PMs and 8-pole synchronous reluctance [17], and the hybrid rotor with the combination of 4- and 8-pole PMs [18].

The PC-MM is designed based on LCF PMs [19][20], of which the polarity can be changed easily, so the excitation field with changeable pole-pair number can be obtained to widen the speed regulation range.

It can be seen that the key difference among these reported PC motors is the generation of excitation field with different pole-pair numbers. FSPM motors operate based on the general air-gap field modulation theory (GAFMT) [21]-[25]. So, there are rich harmonics with different pole-pair numbers in its open-circuit air-gap flux density, which provides a basic condition to achieve the PC design. Namely the PC-FSPM motor can be obtained by using different open-circuit air-gap flux density harmonics for low speed and high speed ranges, respectively. In this paper, a novel PC-FSPM motor with E-core is proposed and optimized. In section II, the operation principle of conventional and PC-FSPM motors is compared based on the GAFMT. In section III, the design process of the proposed motor is introduced. In section IV, a multi-level optimization method is adopted to optimize the performance. In section V, the electromagnetic performances are analyzed by finite element analysis (FEA). In section VI, the prototype is tested to verify the predicted results. In section VII, some conclusions are drawn.

II. PC Principle Analysis Based on the GAFMT

To guide the design of PC-FSPM motor, the operation principle is introduced firstly. According to the GAFMT, a FSPM motor can be normalized into a cascade of three elements,

namely, magnetic source (primitive magneto-motive-force (MMF)), modulator (salient poles) and the filter (armature winding) [23]. Thus, the operation principle of a FSPM motor can be explained in two steps, namely, the generation of working harmonics and the filter action of winding.

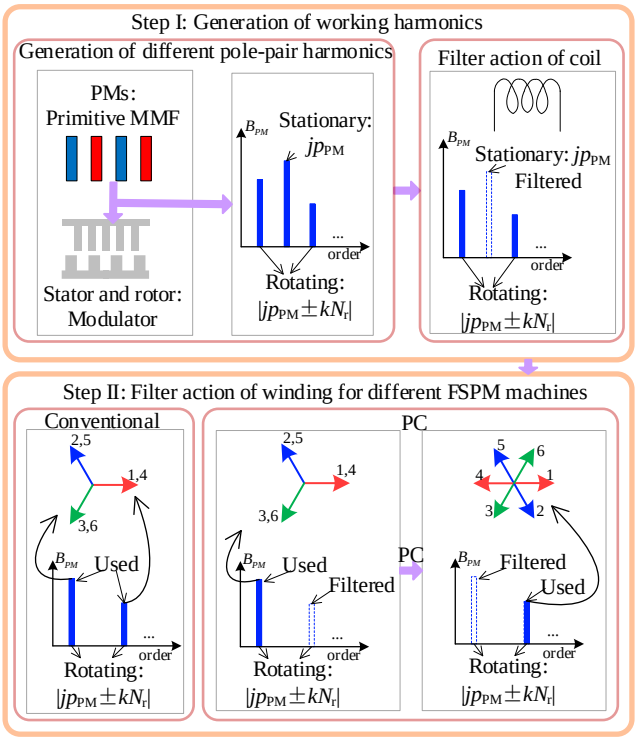

Fig. 1. Operation principle of different FSPM motor.

Firstly, as shown in Step I, Fig. 1, the primitive MMF generated by PMs is modulated by the stator and rotor salient poles, generating rich harmonics in the open-circuit air-gap flux density. The corresponding air-gap flux density can be expressed [21][22] as

$$\begin{cases} B_{PM}(\theta,t) = F_{PM}(\theta)\Lambda_s(\theta)\Lambda_r(\theta,t) \\ \quad = \Lambda_{r0}\sum_{j=1,3,5}^{\infty}[C_{FPMj}\sin(jp_{PM}\theta)] + \\ \quad \frac{1}{2}\sum_{j=1,3,5}^{\infty}\sum_{k=1}^{\infty}[C_{FPMj}C_{\Lambda rk}(\sin\alpha_1+\sin\alpha_2)] \\ \alpha_1 = (jp_{PM}+kN_r)(\theta-\frac{kN_r\omega_r t+\theta_{ini}}{jp_{PM}+kN_r}) \\ \alpha_2 = (jp_{PM}-kN_r)(\theta+\frac{kN_r\omega_r t+\theta_{ini}}{jp_{PM}-kN_r}) \end{cases} \quad (1)$$

where F_{PM}, $\Lambda_s(\theta)$ and $\Lambda_r(\theta, t)$ are PM MMF function, stator and rotor modulation functions, respectively, C_{FPMj} and $C_{\Lambda rk}$ are the Fourier coefficients of PM MMF and rotor modulation function, respectively, Λ_{r0} is the DC component of rotor modulation function, p_{PM}, N_r and ω_r are the pole-pair number of PMs, the rotor tooth number and the rotor speed, respectively, θ_{ini} is the initial position. It can be seen that due to the modulation effect, harmonics with different pole-pair numbers are generated, including stationary and rotating components, which can be classified as shown in Table I.

Then, the winding works as a filter to select specific harmonics to achieve the energy conversion. Specifically, because only the rotating components can produce back-EMF in the coil, the stationary components can be regarded as being filtered out. Among the rotating harmonics, the components with k=1 and j=1, 3, 5, of which the electrical speed is $|N_r\omega_r|$, usually have relatively high amplitudes. So, these components are called main working harmonics in this paper. The filter action of the winding on main working harmonics is the main difference between the conventional and PC FSPM motors, as shown in Step II, Fig. 1.

TABLE I
HARMONICS ANALYSIS OF AIR-GAP FLUX DENSITY

	Pole-pair numbers	Angular speed (Mech.)	Angular speed (Elec.)
Stationary	jp_{PM}	0	0
Rotating	$jp_{PM}+kN_r$	$kN_r\omega_r/(jp_{PM}+kN_r)$	$kN_r\omega_r$
	$jp_{PM}-kN_r>0$	$-kN_r\omega_r/(jp_{PM}-kN_r)$	$-kN_r\omega_r$
	$jp_{PM}-kN_r<0$	$-kN_r\omega_r/(jp_{PM}-kN_r)$	$kN_r\omega_r$

TABLE II
HARMONICS INFORMATION OF DIFFERENT FSPM MOTORS

Motor types	Main harmonics	α	f_W
12/10	4,8,16,20,28,40	2π/3	13.4%
12/11	5,7,17,19,29,41	5π/6	6.7%
12/16	2,10,14,22,34,46	5π/3	13.4%
12/17	1,11,13,23,35,47	11π/6	51.7%

Take conventional 12/10-, 12/11-, 12/16- and 12/17-pole U-core FSPM motors with double layer armature winding as examples, the main working harmonics and the slot pitch angles are listed in Table II. The slot pitch angle is calculated as

$$\alpha = \mathrm{MOD}\left[\mathrm{sign}(\omega_e)\frac{2\pi}{N_s}p_{fh}, 2\pi\right] \quad (2)$$

where sign(ω_e), ω_e and p_{fh} are the rotating direction, electrical speed and pole-pair number of main working harmonics, respectively, and N_s is the stator tooth number. It can be seen that the slot pitch angles of different main working harmonics in each motor are the same, so the coil-EMF vectors drawn according to different main working harmonics in each motor are the same as well. Then a filter capacity factor f_W of the winding on the main working harmonics is defined based on the winding factor, as

$$f_W = [1-\frac{\sin(Q\alpha/2)}{Q\sin(\alpha/2)}\cos(\frac{\theta_c}{2})]\times 100\% \quad (3)$$

where Q is the least EMF vector number per phase, θ_c is phase difference between two slot conductors of one coil. According to the f_W calculated in Table II, the filter capacity on all main working harmonics in each motor are the same. So, all of the main harmonics have to be used or unused simultaneously, which leads to the impossibility of PC operation of conventional FSPM motors.

In order to achieve the PC operation of FSPM motor, the main working harmonics should possess two kinds of slot pitch angle. Thus, based on the different filter capacity of a determined winding on different main working harmonics, specific main working harmonics can be selected for the operation of the motor and the others are filtered out. Then, when the winding configuration is changed, the other main harmonics can be selected. So, the key to achieve a PC-FSPM

motor is to obtain these main harmonics with different slot pitch angles, as shown in Step II, Fig. 1.

III. Design of PC-FSPM Motor

In this section, the slot pole combination and the main working harmonics for PC-FSPM motors are discussed. The design of winding configuration based on the modulated main working harmonics are analyzed as well.

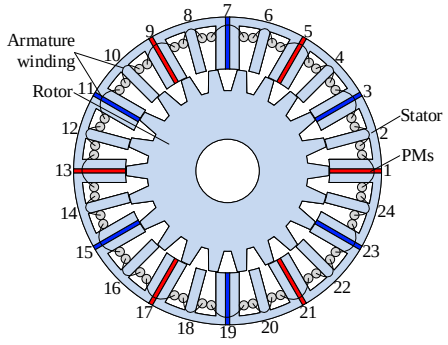

Fig. 2. Configuration of PC-FSPM motor.

A. Selection of the Slot Pole Combination

The feasible slot pole combinations of conventional FSPM motors can be expressed as

$$\begin{cases} N_s = x_1 m, x_1 = 1,2,3... \\ N_r = N_s \pm x_2, x_2 = 1,2,3... \\ p_{PM} = N_s / x_3, x_3 = 2,4 \end{cases} \quad (4)$$

where m is the phase number. The different values of x_3 represent different shaped stator iron core. When x_3=2 and 4, the U- and E-core FSPM motors are formed, respectively.

According to the PC operation principle, the main working harmonics should contain two groups with different slot pitch angles. To achieve the design requirement of using one group of the main working harmonics and filtering the other group, the slot pole commination should meet the requirement of the equation (5) when the double layer winding is adopted.

$$\begin{cases} N_s = 4x_1 m, x_1 = 1,2,3... \\ N_r = x_1(2n+1), n > 0, n \neq 1,4,7,10... \\ p_{PM} = N_s / x_3, x_3 = 4 \end{cases} \quad (5)$$

So, the E-core structure is adopted. Moreover, different from conventional E-core FSPM motors, the stator teeth without PMs are wounded with the windings to satisfy the double layer winding configuration. It can be found that when x_1=1, the unit motor with 12 stator poles can be formed. However, the number of rotor pole is odd, which leads to the unbalanced magnetic force. Therefore, x_1=2 is adopted in this paper. Moreover, to achieve the maximum output torque, N_r should be close to N_s. Finally, the motor with 24/22 slot pole combination is selected, as shown in Fig. 2.

B. Design Process of the Armature Winding

According to the analysis in Section II, the expression of main working harmonics can be expressed as

$$B_{\text{main}}(\theta,t) = \sum B_{p_{fh}} \sin(p_{fh}\theta - \text{sign}(\omega_e)\omega_e t + \theta_{p_{fh}}) \quad (6)$$

where B_{pfh} and θ_{pfh} are the amplitude and phase of the main harmonics, respectively, and the corresponding details are summarized in Table III. It can be seen that the harmonics of different groups have different slot pitch angles, which is consistent with the foregoing analysis.

TABLE III
HARMONICS INFORMATION OF 24/22 PC-FSPM MOTOR

Group	p_{fh}	B_{pfh}	sign(ω_e)	θ_{pfh}	α
I	8	0.27	–	θ_{ini}	4π/3
	16	0.38	+	$-\theta_{\text{ini}}+\pi$	
	40	0.13	+	$-\theta_{\text{ini}}$	
II	4	0.14	+	$-\theta_{\text{ini}}+\pi$	π/3
	28	0.37	+	$-\theta_{\text{ini}}$	
	52	0.3	+	$-\theta_{\text{ini}}$	

TABLE IV
BACK-EMF INFORMATION OF COIL-1

Group	p_{fh}	Amplitude (V)	Phase	Synthesis amplitude	Synthesis phase
I	8	5.32	0	9.59	0
	16	3.74	0		
	40	0.53	0		
II	4	3.32	0	3.99	0
	28	1.20	0		
	52	0.53	π		

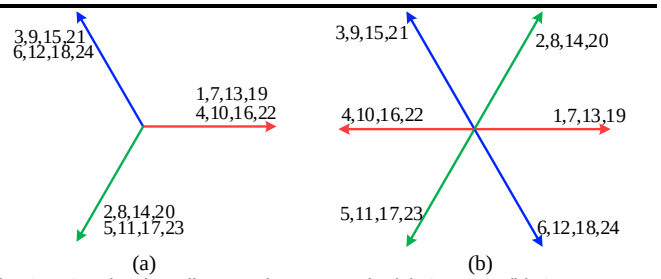

Fig. 3. Synthesis coil EMF phasor graph. (a) Group I. (b) Group II.

TABLE V
WINDING CONFIGURATION AND FILTER CAPACITY FACTOR

	Mode I	Mode II
Phase A	(1+7+13+19)+(4+10+16+22)	(1+7+13+19)-(4+10+16+22)
Phase B	(3+9+15+21)+(6+12+18+24)	(3+9+15+21)-(6+12+18+24)
Phase C	(2+8+14+20)+(5+11+17+23)	(2+8+14+20)-(5+11+17+23)
$f_{W\text{-GI}}$	13.4%	100%
$f_{W\text{-GII}}$	100%	50%

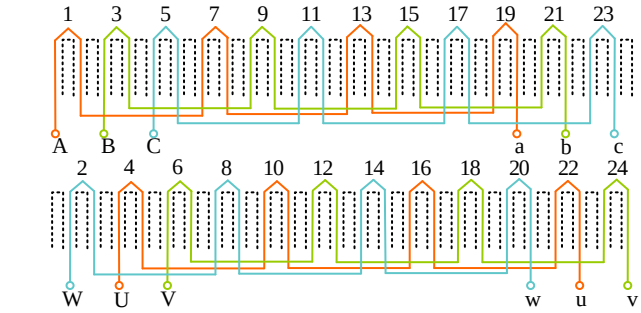

Fig. 4. Dual three-phase winding of PC-FSPM motor.

The back-EMF component produced by each harmonic in each coil can be calculated as

$$e_{coil-i}(t) = \sum \frac{d}{dt}[r_{si} l_a N_{coil} \int_{\theta_{i1}}^{\theta_{i2}} B_{\text{main}}(\theta,t) d\theta] \quad (7)$$

where e_{coil-i} is the back-EMF of the i-th coil, i is the coil number, r_{si} and l_a are the inner radius of the stator and the stack length, respectively, N_{coil} is the turn number per coil, θ_{i1} and θ_{i2} is the mechanical degrees of two winding sides of the i-th coil.

The calculated back-EMF details of the coil-1 due to different harmonics are calculated in Table IV when the speed

is 600 rpm, and the synthesis back-EMF details due to harmonics of each group are presented as well. Accordingly, the synthesis coil back-EMF phasor graph of different harmonic groups can be derived as shown in Fig. 3, based on which the winding configuration to use different harmonic groups can be designed as shown in Table V, and the corresponding filter capacity factors, f_W, are calculated as well. It can be seen that the harmonics in group II are filtered out completely when the winding configuration of Mode I is used. On the contrary, when the winding configuration of Mode II is used, the harmonics in group I are filtered out completely. Therefore, two operating modes can be performed to use different harmonics with different pole-pair numbers to obtain a PC-FSPM motor. Finally, the winding configuration is presented in Fig. 4, which adopts the dual-three phase winding configuration to meet the requirement of changeable winding configuration.

IV. Optimization Of PC-FSPM Motor

To achieve better performance of the PC motor, the main dimension parameters, as defined in Fig. 5, are optimized in this section. The basic design specifications, materials and parameters are listed in Table V.

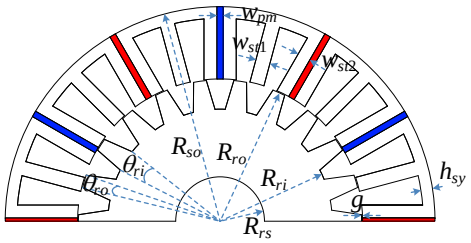

Fig. 5. Dimension Parameters of the PC-FSPM motor.

TABLE VI
BASIC DESIGN SPECIFICATIONS, MATERIALS AND PARAMETERS

Specifications		Materials		
Rated speed	600 rpm	PM	Grade	N35UH
Slot factor	50%		Remanence	1.2 T
Rated current	24 A	Steel	Grade	35WW270
Current density	5 A/mm^2	Copper	Wire size (AWG)	12
Parameters				
Stator outer radius, R_{so}	92 mm		Stack length, l	90 mm
Rotor outer radius, R_{ro}	60.6 mm		Air-gap length, g	0.4 mm

A. Design Objectives

Different from conventional PM motors with single operation mode, there are two operation modes for the proposed PC-FSPM motor, of which Mode I and II are used for high torque condition and high speed condition, respectively. Considering the characteristic of dual operation modes, different design objectives should be considered.

1) Output Torque

According to the operation condition of Mode I, which is for high torque condition, the output torque capacity and torque ripple are chosen as the objectives. The objective function and constraints are presented as

$$\begin{cases} \text{Function}: [\text{Max}\ (T_{out\text{-I}}), \text{Min}\ (T_{rip\text{-I}})] \\ \text{Constraints}: T_{out\text{-I}} \geq 1.2T_{out\text{-}l}, T_{rip\text{-I}} \leq T_{rip\text{-}u} \end{cases} \tag{8}$$

where T_{out} is the output torque, T_{rip} is the torque ripple. $T_{out\text{-}l}$ is the lower limit of output torque, which is calculated according to the torque density, 10 kN/m^3, of conventional PM motors in the natural cooling condition, and $T_{out\text{-}l}$=24 N·m in this paper. $T_{rip\text{-}u}$ is the upper limit of torque ripple, $T_{rip\text{-}u}$=10% here.

Considering Mode II is to expand the speed range, so the objective function is presented as

$$\begin{cases} \text{Function}: [\text{Min}\ (T_{rip\text{-II}})] \\ \text{Constraints}: T_{out-\text{II}} \geq T_{out-\text{I}}/3, T_{rip-\text{II}} \leq T_{rip-u} \end{cases} \tag{9}$$

where the subscripts of I and II represent Mode I and mode II, respectively.

2) Speed Expansion Capability

Apart from the torque optimization, a good speed expansion capability is a critical requirement for a PC motor. The maximum operating speed of a PM motor is limited by the inverter voltage and the current, as

$$i_d^2 + i_q^2 \leq I_{\max}^2 \tag{10}$$

$$(\frac{L_q}{L_d} i_q)^2 + (\frac{\psi_m}{L_d} + i_d)^2 \leq (\frac{U_{\max}}{L_d \omega_e})^2 \tag{11}$$

where i_d, i_q and L_d, L_q are the d- and q-axis current and the d- and q-axis inductance, respectively, $I_{\max}$ and $U_{\max}$ are the peak value of the rated current of motor and the maximum voltage of inverter, respectively, ψ_m is the PM flux linkage.

The voltage limit is an ellipse with the center located at (-ψ_m/L_d,0), of which ψ_m/L_d is defined as the characteristic current. In stator PM motors, $L_d \approx L_q$ [24], so the voltage limit ellipse can be simplified as a circle. With the increasing of the operating speed, the radius of the voltage limit circle decreases gradually. The current and voltage limit circles with different locations of characteristic current point are presented in Fig. 6.

When $\psi_m/L_d > I_{\max}$, the characteristic current point is located outside the current limit circle, as shown in Fig. 6 (a). The maximum reachable operation speed occurs when the voltage and current limit circles are tangent, and can be expressed as

$$\omega_{e\max} = \frac{U_{\max}}{\psi_m + L_d i_{d\max}} = \frac{U_{\max}}{L_d(\psi_m / L_d + i_{d\max})} \tag{12}$$

where $i_{d\max}$ is the maximum flux weakening current, which equals $-I_{\max}$, namely all of the armature current is used for the flux-weakening. It can be seen that maximum reachable speed is related to the characteristic current ψ_m/L_d and L_d.

When $\psi_m/L_d \leq I_{\max}$, the characteristic current point is located inside the current limit circle, as shown in Fig. 6 (b). Therefore, the PM flux can be counteracted totally by the flux-weakening field generated by i_d, which means the motor possesses an excellent flux-weakening capability under this condition and the maximum operating speed is infinite theoretically. However, as can be seen from the phasor diagram under i_d=0 control in Fig. 7, when the winding resistance is ignored, the power factor can be calculated as

$$\cos\theta = 1/\sqrt{1 + \frac{L_q}{\psi_m} i_q} \approx 1/\sqrt{1 + \frac{L_d}{\psi_m} i_q} \tag{13}$$

It can be seen the power factor is proportional to the characteristic current value ψ_m/L_d, which means a smaller characteristic current value leads to a smaller power factor.

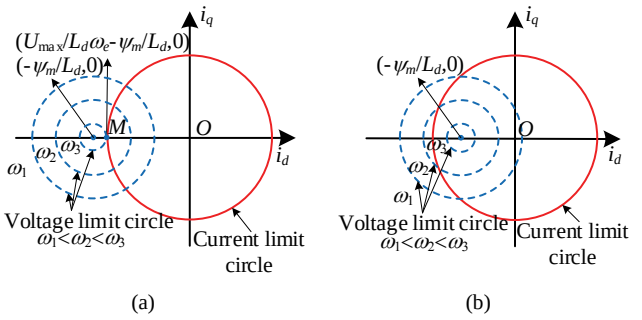

Fig. 6. Current and voltage circles. (a) $\psi_m/L_d \le I_{max}$. (b) $\psi_m/L_d > I_{max}$.

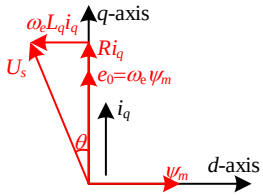

Fig. 7. Phasor diagram of the PM motor under i_d=0 control.

In summary, the characteristic current value determines both the speed expansion capability and the power factor of the motor. Therefore, the characteristic current point should be designed outside and away from the current limit circle under Mode I to achieve higher power factor and output torque. Moreover, the characteristic current point of Mode II is designed outside the current limit circle as well and the maximum operation speed of Mode II should be designed as large as possible. So, a speed range factor is defined as

$$k_{se-\mathrm{II}} = 1/\left(\psi_{m-\mathrm{II}} + L_{d-\mathrm{II}} i_{d\max}\right) \tag{14}$$

Accordingly, the objective function and constraints are presented as

$$\begin{cases} \text{Function}: [\text{Max}\ (I_{\text{char-I}}), \text{Max}\ (k_{se-\mathrm{II}})] \\ \text{Constraints}: I_{\text{char-I}} \ge I_{\max}, I_{\text{char-II}} \ge I_{\max} \end{cases} \tag{15}$$

where $I_{\text{char-I}}$ and $I_{\text{char-II}}$ are the characteristic current of Mode I and II.

B. Optimization Process

Since the proposed motor possess two operation modes and multiple objectives, the existing optimization method for conventional motors cannot be adopted directly. So, a multi-level optimization method is adopted and the flowchart of the optimization process is presented in Fig. 8. The specific optimization process can be expressed as follow.

Step 1: Determine the variation ranges of design parameters. The variation ranges of design parameters are listed in Table VII.

TABLE VI
VARIATION RANGES OF DESIGN PARAMETERS

Parameters	Variation range
Rotor inner radius, R_{ri}	[46 mm,50 mm]
Rotor outer arc, θ_{ro}	[4°,6°]
Rotor inner arc, θ_{ri}	[10°,12°]
PM width, w_{pm}	[2.2 mm,2.8 mm]
Stator tooth shoe 1 width, w_{st1}	[2 mm,8mm]
Stator tooth shoe 2 width, w_{st2}	[2 mm,6 mm]
Stator yoke height, h_{sy}	[5 mm, 7 mm]

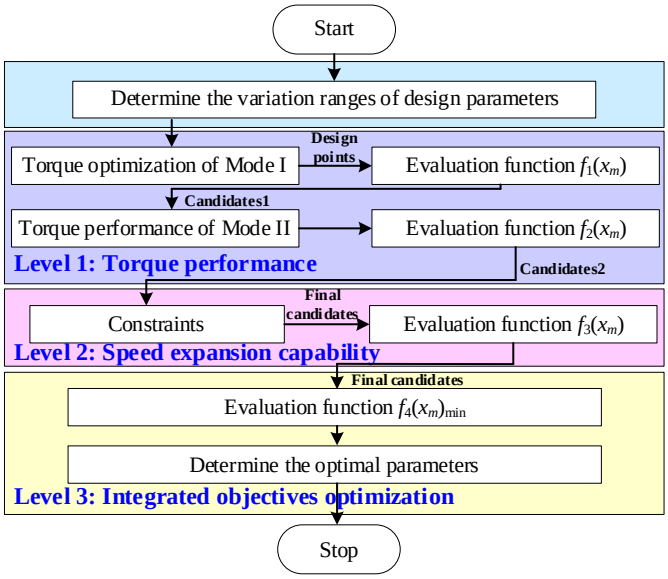

Fig. 8. The flowchart of the optimization process.

Step 2: Optimization process of level 1. In level 1, the design objectives of torque performance are considered. Firstly, the torque design objectives optimization of Mode I is carried out to obtain the design points. Then the evaluation function $f_1(x_m)$ is introduced to select the candidate 1 for the torque optimization of Mode II. In this way, the time consumption of the optimization of Mode II can be reduced greatly. According to the evaluation function $f_2(x_m)$, the candidate 2 can be selected for the level 2 optimization process. The candidates 1 and 2 are determined according to the top 20% of $f_1(x_m)$ and $f_2(x_m)$. The evaluation function $f_1(x_m)$ and $f_2(x_m)$ are expressed as

$$\begin{cases} f_1(x_m) = \lambda_{1-1}\dfrac{T'_{out-\mathrm{I}}}{T_{out-\mathrm{I}}(x_m)} + \lambda_{1-2}\dfrac{T_{rip-\mathrm{I}}(x_m)}{T'_{rip-\mathrm{I}}} \\ \lambda_{1-1} = \lambda_{1-2} = 0.5 \end{cases} \tag{16}$$

$$f_2(x_m) = \lambda_{2-1}\frac{T_{rip-\mathrm{II}}(x_m)}{T'_{rip-\mathrm{II}}}, \lambda_{2-1} = 1 \tag{17}$$

where $\lambda_{1\text{-}1}$, $\lambda_{1\text{-}2}$ and $\lambda_{2\text{-}1}$ are the weight coefficient, T'_{out} and T'_{rip} are the output torque and torque ripple values of the initial design point, $T_{out}(x_m)$ and $T_{rip}(x_m)$ are the values of different design points.

Step 3: Optimization process of level 2. In level 2, the design objectives of speed expansion capability are considered. According to the constraints in (15), the final candidates are determined firstly. Then the evaluation function $f_3(x_m)$ is introduced as

$$\begin{cases} f_3(x_m) = \lambda_{3-1}\dfrac{I'_{\text{char}-\mathrm{I}}}{I_{\text{char}-\mathrm{I}}(x_m)} + \lambda_{3-2}\dfrac{k'_{se-\mathrm{II}}}{k_{se-\mathrm{II}}(x_m)} \\ \lambda_{3-1} = \lambda_{3-2} = 0.5 \end{cases} \tag{18}$$

where $\lambda_{3\text{-}1}$and $\lambda_{3\text{-}2}$ are the weight coefficient, I'_{char} and k'_{se} are the characteristic current and speed expansion capability factor of the initial design point, $I_{\text{char}}(x_m)$ and $k_{se}(x_m)$ are the values of different design points.

Step 4: Optimization process of level 3. In level 3, the integrated objectives optimization is carried out. Namely, all of the design objectives of different modes are considered

according to the evaluation function $f_4(x_m)$, which can be expressed in (19), and the final parameters can be determined.

$$\begin{cases} f_4(x_m)_{\min} = \lambda_{4-1}\dfrac{f_1(x_m)}{f'_1} + \lambda_{4-2}\dfrac{f_2(x_m)}{f'_2} + \lambda_{4-3}\dfrac{f_3(x_m)}{f'_3} \\ \lambda_{4-1} = \lambda_{4-2} = \lambda_{4-2} = 1/3 \end{cases} \quad (19)$$

where $\lambda_{4\text{-}1}$, $\lambda_{4\text{-}2}$ and $\lambda_{4\text{-}3}$ are the weight coefficient, f'_1, f'_2 and f'_3 are the f_1, f_2 and f_3 values of the initial design point.

C. Optimization Results

The optimization results can be derived as follows. Firstly, the initial design points are determined according to (8), and the corresponding evaluation function values and candidates 1 are presented in Fig. 9. It can be seen that with the selection of evaluation function $f_1(x_m)$, the candidate design points are reduced greatly. Then the torque performance of Mode II of candidates 1 are presented in Fig. 10 and candidates 2 points are selected. The characteristic current value of Mode I and $k_{se\text{-}II}$ of the candidates 2 are shown in Fig. 11. Moreover, the optimal design point can be determined according to minimal $f_4(x_m)$ as shown in Fig. 11, and the optimal parameter values are concluded as R_{ri}=48 mm, θ_{ro}=5.2°, θ_{ri}=11.2°, w_{pm}=2.6 mm, w_{st1}=6.2 mm, w_{st2}=5.6 mm, h_{sy}=5 mm.

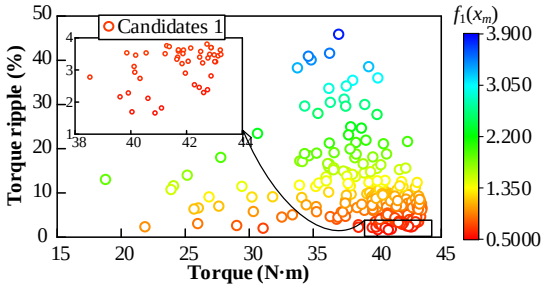

Fig. 9. Initial design points and candidate 1 points.

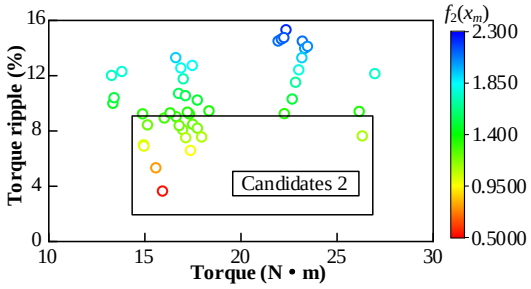

Fig. 10. Candidate 2 points.

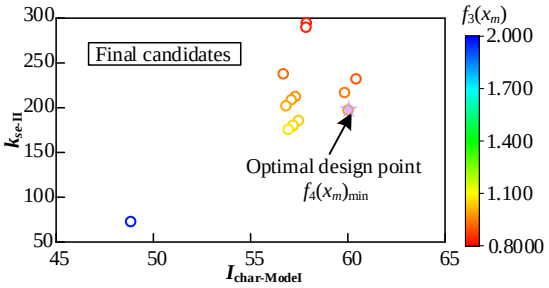

Fig. 11. Final candidate points and optimal design points.

V. Electromagnetic Performance

To verify the feasibility of the proposed PC-FSPM motor, the electromagnetic performance is calculated by 2-D FEA

A. No-load Performance

The air-gap flux density waveform and the harmonic spectrums are presented in Fig. 12. It can be seen that the air-gap flux density is mainly caused by the stationary harmonics with the pole-pair number of 6, 18 and 30 when k=0, the rotating harmonics with the pole-pair number of 4, 8, 16, 28, 40 and 52 when k=1, which is consistent with the analysis in Section III.

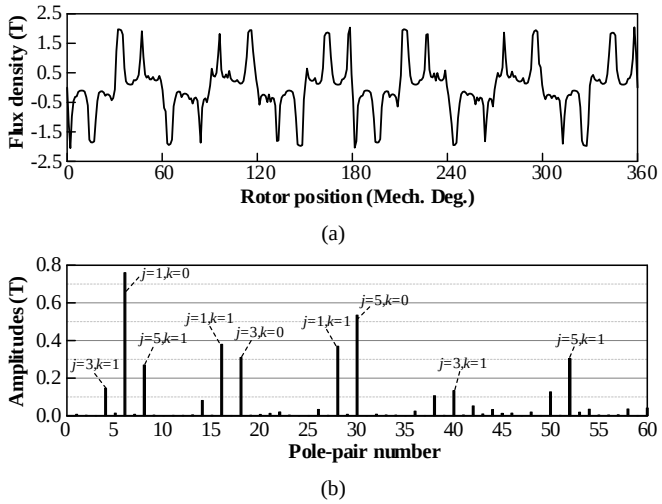

Fig. 12. Air-gap flux density. (a) Waveform. (b) Harmonic spectrums

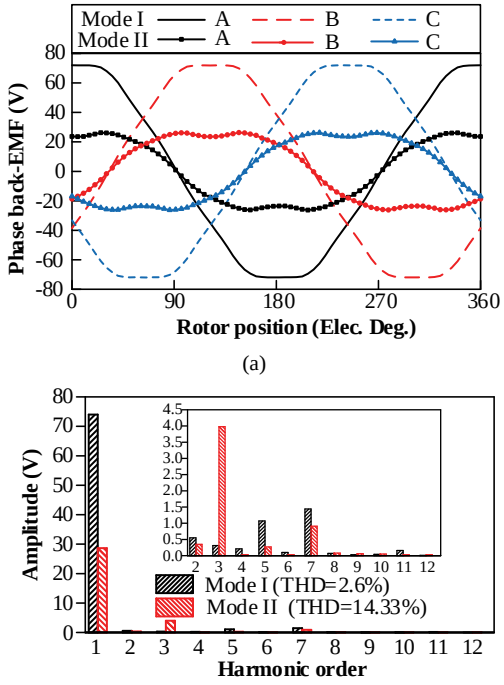

Fig. 13. Back-EMF. (a) Waveform. (b) Harmonic spectrums.

The no-load back-EMF waveform and the harmonic spectrums at 600 rpm are presented in Fig. 13. It can be found that the back-EMF can be regulated effectively. The fundamental amplitude of Mode II is 0.38 times of Mode I, which are beneficial for high torque of Mode I and high speed operation of Mode II, respectively. Furthermore, the total harmonic distortion (THD) of Mode I is small, which ensures the lower torque ripple of this mode. Moreover, it can be found that apart from the relatively higher 3rd harmonic of Mode II, the THD of Mode II is very small as well. Therefore, the lower

torque ripple of Mode II can be ensured as well due to the 3rd back-EMF harmonic does not generate output torque ripple.

With the PC operation, the inductance characteristic of different modes is changed as shown in Fig. 14. It can be found that the *d*- and *q*-axis inductances are decreased from Mode I to Mode II, and the *d*-axis inductance of Mode II is 0.73 times of Mode I. Therefore, with the variation of the back-EMF，namely PM flux linkage, and the *d*-axis inductance, the expanded speed range can be achieved. Moreover, it can be seen that the saliency effect of Mode I and II is relatively low.

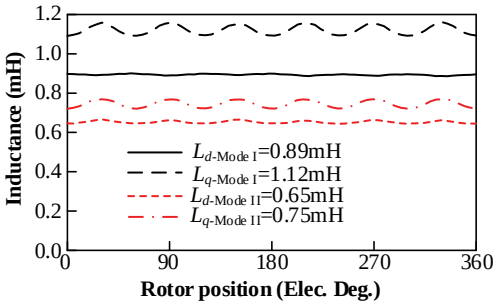

Fig. 14. The *dq*-axis inductance waveform.

B. Torque Performance

When rated current is fed, the average torque against different current angle under different modes is shown in Fig. 15. The current angle is defined as the phase difference between the phase current and back-EMF. As can be seen, the maximum output torque is achieved when the current angle is around 0°, indicating the saliency effect is relatively low, and the reluctance torque is negligible. Therefore, the i_d=0 control strategy is more suitable to achieve the maximum output torque. The torque waveforms of different modes when i_d=0 control strategy is adopted are presented in Fig. 16. As can be seen, the output torque can be regulated effectively with PC operation. Moreover, the torque ripple of different modes is very small.

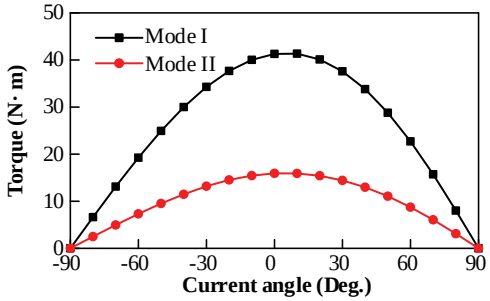

Fig. 15. Average torque against different current angle.

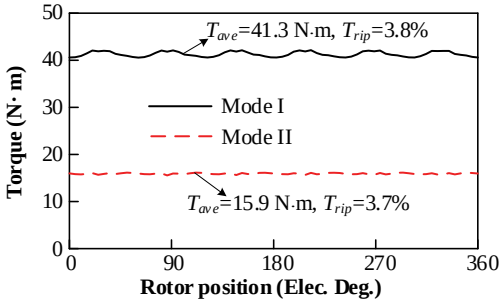

Fig. 16. Output torque waveform.

C. Speed Expansion Performance

To verify the speed expansion performance of the proposed PC motor, the torque-speed curve under 150V DC bus voltage is presented in Fig. 17. It can be found that the speed expansion range of Mode I is very small to ensure the output torque capacity and higher power factor. When the motor switches from Mode I to Mode II, the output torque is reduced to 38% of Mode I, and the speed expansion is expanded from 3 times rated speed to 10 times rated speed.

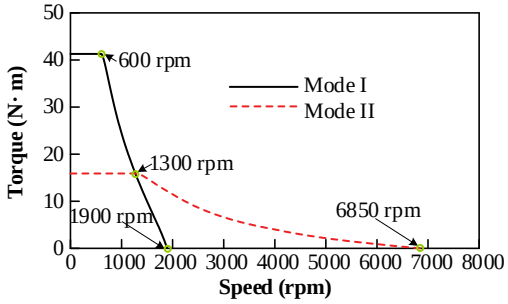

Fig. 17. Torque-speed curves.

VI. Experimental Verification

To validate the feasibility of the proposed motor, a prototype is built as shown in Fig. 18.

Fig. 18. Prototype. (a) Silicon steel sheet. (b) Stator. (c) Rotor.

The back-EMF at 600 rpm in different modes are tested and compared with FEA predication as shown in Fig. 19. As can be seen, the tested results agree well with the predicated ones, although the fundamental amplitudes are a little smaller, which is mainly caused by the end-effect, manufacturing imperfection and measurement errors.

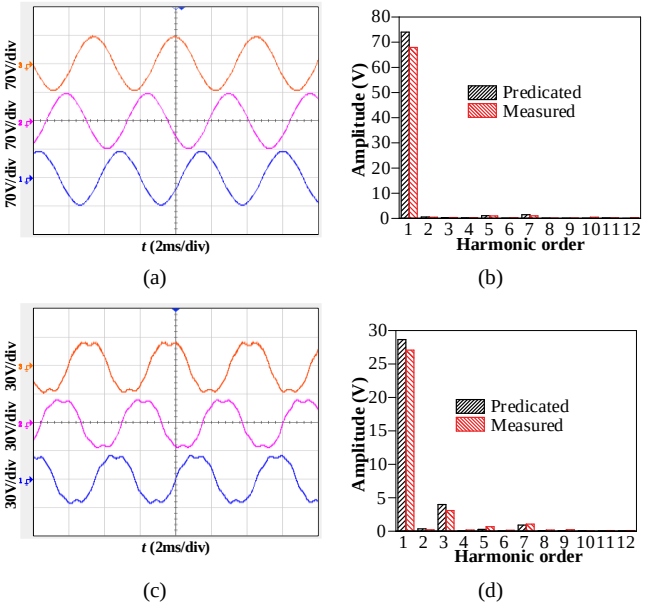

Fig. 19. Back-EMF at 600rpm. (a) Measured waveform of Mode I. (b) Harmonic spectrums of Mode I. (c) Measured waveform of Mode II. (d)

Harmonic spectrums of Mode II.

Further, the test platform is established as shown in Fig. 20 to verify the torque performance. The response with changing load of Mode I and II is tested firstly as shown in Fig. 21. As can be seen, when the load is changed from 12.3 to 25.5 to 37.3 N·m in Mode I, and from 4.8 to 9.6 to 14.5 N·m in Mode II, the phase current is varied from 1/3 to 2/3 to 1 times rated current. According to the FEA results, the corresponding currents can generate 13.9 N·m, 27.7 N·m, 41.3 N·m output torque in Mode I, and 5.4 N·m, 10.7 N·m, 15.9 N·m output torque in Mode II, respectively. The measured torque is always about 90% of the FEA values. Fig. 22 presents the response with changing speed from 200 to 600 rpm with the phase current of 12 A. It can be seen from the transient response waveforms that the proposed motor possesses a well dynamic response under different modes.

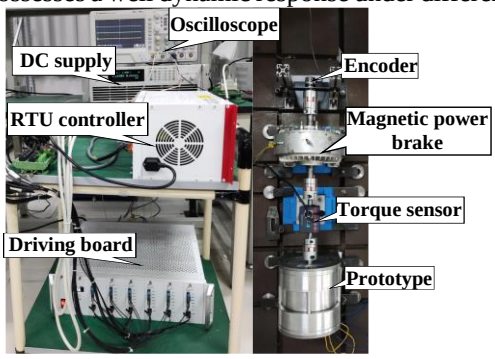

Fig. 20. Test platform of the proposed motor.

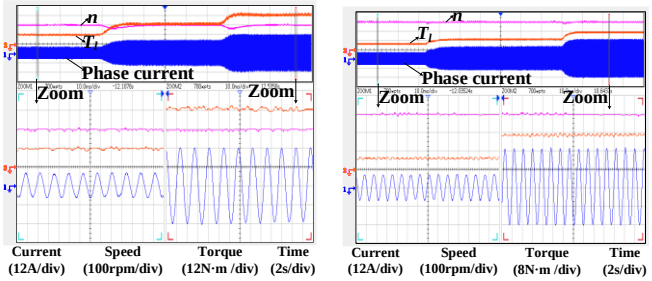

(a) (b)

Fig. 21. Changing load response. (a) Mode I. (b) Mode II.

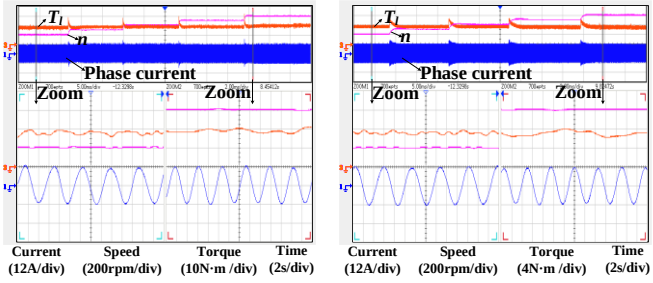

(a) (b)

Fig. 22. Changing speed response. (a) Mode I (b) Mode II.

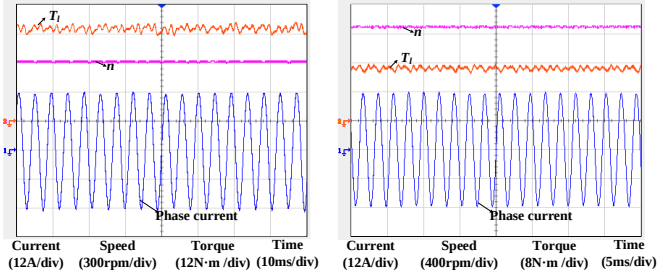

(a) (b)

Fig. 23. Steady waveforms. (a) Mode I. (b) Mode II.

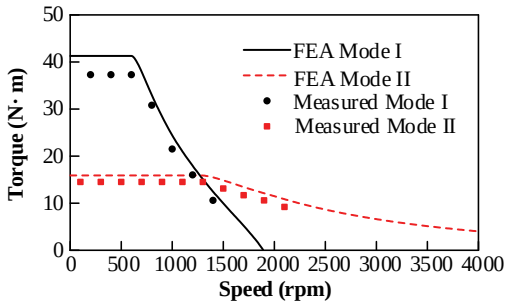

Fig. 24. Torque speed curves of different modes.

The steady waveforms in Mode I at 600 rpm and in Mode II at 1300 rpm with rated current is shown in Fig. 23. It can be found that the proposed motor can operates steadily. Finally, the torque-speed curve is tested as shown in Fig. 24. It can be seen that the test results matches well with the FEA results.

VII. Conclusion

This paper introduces the conventional PC method in the design of the FSPM motor to meet the requirement of high torque density and wide speed regulation range. With the field modulation effect inherited in the FSPM motor, the air-gap flux density harmonics with different pole-pair numbers are generated. By adopting appropriate slot pole combinations, the excitation harmonics of FSPM motor with different slot pitch angle can be obtained. Then by using different harmonics with different winding configuration, the PC-FSPM motor can be designed to possess different operating modes for high torque condition and high speed condition, respectively.

Based on the GAFMT, the operation principle of the conventional and PC-FSPM motors is compared. Besides, a 24/22-pole PC-FSPM motor with E-shaped iron core is proposed and optimized. According to the electromagnetic performance results, the torque density is 17.3 kN/m^3 in the natural cooling condition, which is higher than the 10 kN/m^3 of the conventional PM motors. Moreover, the motor can operate 10 times rated speed. In other word, the proposed motor can achieve high torque and wide speed range at the same time.

References

[1] M. Cheng, W. Hua, J. Zhang, and W. Zhao, "Overview of stator-permanent magnet brushless machines," *IEEE Trans. Ind. Electron.*, vol. 58, no. 11, pp. 5087-5101, Nov. 2011.

[2] Z. Z. Wu and Z. Q. Zhu, "Analysis of air-gap field modulation and magnetic gearing effects in switched flux permanent magnet machines," *IEEE Trans. Magn.*, vol. 51, no. 5, May 2015, Art no. 8105012.

[3] H. Chen, A. M. EL-Refaie and N. A. O. Demerdash, "Flux-switching permanent magnet machines: A review of opportunities and challenges—Part I: Fundamentals and topologies," *IEEE Trans. Energy Conver.*, vol. 35, no. 2, pp. 684-698, June 2020.

[4] R. Cao, C. Mi and M. Cheng, "Quantitative comparison of flux-switching permanent-magnet motors with interior permanent magnet motor for EV, HEV, and PHEV applications," *IEEE Trans. Magn.*, vol. 48, no. 8, pp. 2374-2384, Aug. 2012.

[5] W. Hua, G. Zhang and M. Cheng, "Flux-regulation theories and principles of hybrid-excited flux-switching machines," *IEEE Trans. Ind. Electron.*, vol. 62, no. 9, pp. 5359-5369, Sept. 2015.

[6] G. Zhang, W. Hua, M. Cheng and J. Liao, "Design and comparison of two six-phase hybrid-excited flux-switching machines for EV/HEV applications," *IEEE Trans. Ind. Electron.*, vol. 63, no. 1, pp. 481-493, Jan. 2016.

[7] H. Hua and Z. Q. Zhu, "Novel partitioned stator hybrid excited switched flux machines," *IEEE Trans. Energy Conver.*, vol. 32, no. 2, pp. 495-504, June 2017.
[8] H. Yang, Z. Q. Zhu, H. Lin and S. Lyu, "Comparative study of hybrid pm memory machines having single- and dual-stator configurations," *IEEE Trans. Ind. Electron.*, vol. 65, no. 11, pp. 9168-9178, Nov. 2018.
[9] Z. Q. Zhu, M. M. J. Al-Ani, X. Liu and B. Lee, "A mechanical flux weakening method for switched flux permanent magnet machines," *IEEE Trans. Energy Conver.*, vol. 30, no. 2, pp. 806-815, June 2015.
[10] S. Mallampalli, Z. Q. Zhu, J. C. Mipo and S. Personnaz, "Six-phase pole-changing winding induction machines with improved performance," *IEEE Trans. Energy Conver.*, vol. 36, no. 1, pp. 534-546, March 2021.
[11] E. F. Fuchs, J. Schraud and F. S. Fuchs, "Analysis of critical-speed increase of induction machines via winding reconfiguration with solid-state switches," *IEEE Trans. Energy Conver.*, vol. 23, no. 3, pp. 774-780, Sept. 2008.
[12] B. S. Umesh and K. Sivakumar, "Multilevel inverter scheme for performance improvement of pole-phase-modulated multiphase induction motor drive," *IEEE Trans. Ind. Electron.*, vol. 63, no. 4, pp. 2036-2043, April 2016.
[13] H. Nam, S. -K. Jung, G. -H. Kang, J. -P. Hong, T. -U. Jung and S. -M. Baek, "Design of pole-change single-phase induction motor for household appliances," *IEEE Trans. Ind. Appl.*, vol. 40, no. 3, pp. 780-788, May-June 2004.
[14] M. -S. Lim and J. -P. Hong, "Design of high efficiency wound field synchronous machine with winding connection change method," *IEEE Trans. Energy Conver.*, vol. 33, no. 4, pp. 1978-1987, Dec. 2018.
[15] E. Libbos, B. Ku, S. Agrawal, S. Tungare, A. Banerjee and P. T. Krein, "Loss minimization and maximum torque-per-ampere operation for variable-pole induction machines," *IEEE Trans. on Transport. Electrific.*, vol. 6, no. 3, pp. 1051-1064, Sept. 2020.
[16] F. J. Haddad Kalluf, L. N. Tutelea, I. Boldea and A. Espindola, "2/4-pole split-phase capacitor motor for small compressors: A comprehensive motor characterization," *IEEE Trans. Ind. Appl.*, vol. 50, no. 1, pp. 356-363, Jan.-Feb. 2014.
[17] A. D. Aliabad and F. Ghoroghchian, "Design and analysis of a two-speed line start synchronous motor: Scheme one," *IEEE Trans. Energy Conver.*, vol. 31, no. 1, pp. 366-372, March 2016.
[18] F. Ghoroghchian, A. Damaki Aliabad and E. Amiri, "Two-speed line start permanent magnet synchronous motor with dual magnetic polarity," *IEEE Trans. Ind. Appl.*, vol. 54, no. 5, pp. 4268-4277, Sept.-Oct. 2018.
[19] N. Yuzawa and K. Sakai, "A permanent magnet motor capable of pole changing for variable speed drive," 2013 *Int. Conf. Electr. Mach. and Syst.* (ICEMS), 2013, pp. 1127-1132.
[20] F. Li, K. T. Chau and C. Liu, "Pole-changing flux-weakening dc-excited dual-memory machines for electric vehicles," *IEEE Trans. Energy Convers.*, vol. 31, no. 1, pp. 27-36, March 2016.
[21] Y. Du et al., "Comparison of flux-switching PM motors with different winding configurations using magnetic gearing principle," *IEEE Trans. Magn.*, vol. 52, no. 5, pp. 1-8, May 2016, Art no. 8201908.
[22] P. Wang, W. Hua, G. Zhang, B. Wang and M. Cheng, "Principle of flux-switching permanent magnet machine by magnetic field modulation theory part i: back-electromotive-force generation," *IEEE Trans. Ind. Electron.*, vol. 69, no. 3, pp. 2370-2379, March 2022.
[23] M. Cheng, P. Han, and W. Hua, "General airgap field modulation theory for electrical motors," *IEEE Trans. Ind. Electron.*, vol. 64, no. 8, pp. 6063-6074, Aug. 2017.
[24] P. Wang, W. Hua, G. Zhang, B. Wang and M. Cheng, "Inductance characteristics of flux-switching permanent magnet machine based on general air-gap filed modulation theory," *IEEE Trans. Ind. Electron.*, vol. 69, no. 12, pp. 12270-12280, Dec. 2022.
[25] Y. Du, Y. Mao, F. Xiao, X. Zhu, Y. Sun and L. Quan, "A Pole-Changing Doubly Salient Permanent Magnet Motor," *IEEE Trans. on Transport. Electrific.*, vol. 8, no. 2, pp. 2479-2489, June 2022.

Yi Mao received the B.S. degree in automation from Luoyang Institute of Science and Technology, Luoyang, China, in 2017. He is currently working toward the Ph.D. degree in electrical engineering in Jiangsu University, Zhenjiang, China.

His research interests include motor design and sensorless control of PM motor.

Yi Du (S'10-M'14) received the B.Sc. and M.Sc. degrees in electrical engineering from Jiangsu University, Zhenjiang, China, in 2002 and 2007, respectively, and Ph. D. degree in electrical engineering from Southeast University, Nanjing, China, in 2014.

He is currently a professor in School of Electrical and Information Engineering. His research interests include design and analyze electric machines.

Feng Xiao received the B.Sc., M.Sc. and Ph. D. degrees in electrical engineering from Jiangsu University, Zhenjiang, China, in 1998, 2007 and 2020, respectively. Since 2008, she has been with Jiangsu University, where she is currently senior experimentalist in School of Mechanical Engineering, Jiangsu University.

Her current research interests include design, analysis, and drive control of novel permanent magnet motor with low speed and high torque for direct drive systems.

Xiaoyong Zhu (M'09) received the B.Sc. and M.Sc. degrees from Jiangsu University, Zhenjiang, China, in 1997 and 2002, respectively, and the Ph.D. degree from the School of Electrical Engineering, Southeast University, Nanjing, China, in 2008, all in electrical engineering.

He is currently a Professor with the School of Electrical Information Engineering. His current research interests include design and drive control of electric machines.

Li Quan received the B.Sc. degree from Hefei University of Technology, Hefei, China, in 1985, the M.Sc. degree from Southeast University, Nanjing, China, in 1991 and the Ph.D. degree from Nanjing University of Aeronautics and Astronautics, Jiangsu, China, in 2007.

He is currently a Professor in the School of Electrical and Information Engineering. His research interests include hybrid electric vehicles and motor drive control.